IOP Publishing Physics in Medicine and Biology

Phys. Med. Biol. **52** (2007) 3531–3547 doi:10.1088/0031-9155/52/12/013

# Ultrasonic tissue characterization for monitoring nanostructured $TiO_2$-induced bone growth

**G Rus**[1] **and J García-Martínez**[2]

[1] Department of Structural Mechanics, University of Granada, Politécnico de Fuentenueva, 18071 Granada, Spain
[2] Department of Inorganic Chemistry, University of Alicante, E-03690 Alicante, Spain

E-mail: grus@ugr.es

Received 13 September 2006, in final form 13 April 2007
Published 22 May 2007
Online at stacks.iop.org/PMB/52/3531

**Abstract**

The use of bioactive nanostructured $TiO_2$ has recently been proposed for improving orthopaedic implant adhesion due to its improved biocompatibility with bone, since it induces: (i) osteoblast function, (ii) apatite nucleation and (iii) protein adsorption. The present work focuses on a non-ionizing radiation emitting technique for quantifying in real time the improvement in terms of mechanical properties of the surrounding bone due to the presence of the nanostructured $TiO_2$ prepared by controlled precipitation and acid ageing. The mechanical strength is the ultimate goal of a bone implant and is directly related to the elastic moduli. Ultrasonics are high frequency mechanical waves and are therefore suited for characterizing elastic moduli. As opposed to echographic techniques, which are not correlated to elastic properties and are not able to penetrate bone, a low frequency ultrasonic transmission test is proposed, in which a P-wave is transmitted through the specimen and recorded. The problem is posed as an inverse problem, in which the unknown is a set of parameters that describe the mechanical constants of the sequence of layers. A finite element numerical model that depends on these parameters is used to predict the transformation of the waveform and compare to the measurement. The parameters that best describe the real tissue are obtained by minimizing the discrepancy between the real and numerically predicted waveforms. A sensitivity study to the uncertainties of the model is performed for establishing the feasibility of using this technique to investigate the macroscopic effect on bone growth of nanostructured $TiO_2$ and its beneficial effect on implant adhesion.

(Some figures in this article are in colour only in the electronic version)

  

## 1. Introduction

There is an increasing number of elderly people that suffer from limitations of orthopaedic implants. Current metal-based orthopaedic implants technology (e.g. titanium, which presents good biocompatibility and mechanical properties) is limited to an average lifetime of 10–15 years. After this period, implants fail by debonding from the bone. By this time, the patient is 10–15 years older and may have to choose between the risk of a major surgery or resigning mobility. In the UK, 200 operations are held every year for failed hip implant replacements, accounting for complications such as thrombotic accidents or disability (Gonzalez and Mekhail 2004, Haydon *et al* 2004).

Just to give some figures, 1.5 million bone fractures per year are attributed to osteoporosis (National Osteoporosis Foundation 2003). The percentage of the population older than 65 will increase from 12.4% to 23% between 2000 and 2100 (US Census Bureau 2003). Accordingly, the number of osteoporosis cases is expected to rise from 10 to 14 million from 2000 to 2020 (National Osteoporosis Foundation 2003) or, in other words, osteoporosis-related fractures will triple in the next 60 years (National Osteoporosis Foundation 2003).

To study the limitation in the lifetime, we should focus on the interface between the implant and the bone. This part requires substitute materials to serve as artificial or natural induced bone. The medical applications provide, in addition to a great challenge, a direct way in which engineering can help medical science. This constitutes a specific application of the monitorization of these structures, first in laboratory and, in the future, *in vivo*.

One of the most successful approaches used to improve implant lifetime is the introduction of controlled roughness on the implant surface (Palin *et al* 2005, Webster *et al* 2001b, Gutwein and Webster 2003). Three main reasons have been suggested to justify the better bond adhesion and overall lifetime observed in implants with nanostructured surfaces (Palin *et al* 2005, Keshmiri and Troczynski 2003):

- Implants that better mimic the surface of natural bonds induce a more efficient osteoblast (bone-forming cells) function.
- A higher density of Ti–OH groups on the implant surface favours apatite nucleation.
- Implants with higher surface area increase the protein adsorption (needed for osteoblast adhesion).

A wide variety of techniques have been used to produce controlled implant surface roughness including chemical etching, sol–gel precipitation, anodization, and the incorporation of nanoparticles or nanostructured materials (Webster *et al* 2001b, Keshmiri and Troczynski 2003, de Oliveira and Nancy 2004, Lear Swan *et al* 2005, Dieudonné *et al* 2002, Bayoumi and Ateya 2006, Lee *et al* 2006). Titanium being one of the most widely used metals for implants, since its introduction by Branemark *et al* (1977), nanostructured titanium oxide (titania) has been specifically used to improve bond adhesion and overall implant lifetime (Hazan *et al* 1993, Zhu *et al* 2004, Webster *et al* 1999, 2001a). Several studies show that those titania materials, whose surface roughness better mimic the surface of natural bond, are more efficient at increasing osteoblast function (Palin *et al* 2005, Gutwein and Webster 2003, Webster *et al* 1999, 2000, 2001a).

This paper intends to fill the gap between the material science behind the nanoscale phenomena described above and the ultimate mechanical resistance of the induced new bone in real human cases. Among the current technologies to monitor and characterize the material science phenomena, the most popular are acoustic force microscopy, scanning electron microscopy, x-ray diffraction or transmission electron microscopy. If we focus on the human *in vivo* scale, there are available techniques such as magnetic resonance imaging,

computer-assisted tomography or dual energy x-ray absorption. These are still limited to verify the performance of new bone during the healing period. For this reason, ultrasonic elastography is proposed, since it allows continuous monitoring over the healing period, it involves no ionizing radiation and it is inexpensive.

Elastography is a suitable technique to assess local mechanical properties of tissue. In its classical form, this technique has been developed mainly in the laboratory and consists in applying a quasistatic compression force that causes a strain field of about 1%, which is measured by ultrasound (or RF) tissue motion imaging. The strain field from the applied compression is contaminated by considerable tissue motions from patient movement, breath and cardiac dynamics. The application of the compression is limited to a specific shape, and the distribution of the stress field is not uniform due to the different tissue constants, especially between fibrous and fatty tissue. All this degrades and limits the precision of the technique.

The proposed procedure to quantify the elasticity is based on an entirely different principle: an ultrasonic transmission is set up and the complete waveform is recorded after travelling through the set of tissue layers. The propagation attenuation and velocity depend on the frequency and the mechanical properties of the tissue. The problem is posed as an inverse problem, in which the unknown is a reduced set of parameters that describe the mechanical constants of the sequence of layers, which are selected by means of the parametrization. A finite element numerical model that depends on the parameters is used to predict the transformation of the waveform and compare to the measurement. The value of the parameters that best describe the real tissue is obtained by minimizing the discrepancy or misfit between the real and numerically predicted waveforms. This is done by defining a scalar cost functional from this discrepancy and minimizing it for the parameters. It should be noted that the correct choice of the cost functional definition, the parametrization and the magnitude to compare are the three crucial decisions to pose a robust inverse problem.

In the past decade, elasticity imaging has emerged as a complementary technique to ultrasonic imaging (see the review by Wells (2006), section 3.2). Several reviews of the practical experience with this technique were made by Ophir *et al* (2002a, 2002b) or later by Konofagou (2004). Many physicists' confidence in the future availability of commercial elastography is evidenced by the new manual for residents in elasticity imaging by Hall (2003). Kallel and Bertrand (1996) tackle the elasticity reconstruction for the first time by an inverse problem using a finite element model. The regularization is achieved by a classical Tikhonov scheme, which provides *a priori* information for the solution. Miga (2003) and Doyley *et al* (2005) provide a similar inversion from elastographic images. A good survey of the present challenges in ultrasonics for medical diagnosis is provided by Hill *et al* (2004), with interesting contributions in multiscale relationships, bioeffects and biophysics of soft tissue. Righetti *et al* (2004) use standard elastographic procedures to determine the temporal Poisson's ratio of porous media subjected to pressure, and therefore obtain information about the permeability, which may be useful for correlating with the pathological conditions.

## 2. Methodology

### *2.1. Ultrasonics*

Instead of the echogenic principle that is the base for most current techniques, a transmission setup (using a separate transmitter and receiver) is proposed, where the complete waveform, transmitted and propagated through the specimen, is recorded at the receiver for its inversion, in order to find some elastic constants in the specimen. The velocity and attenuation variation are dependent on the frequency and elastic constants of the layers that the wave travels through.

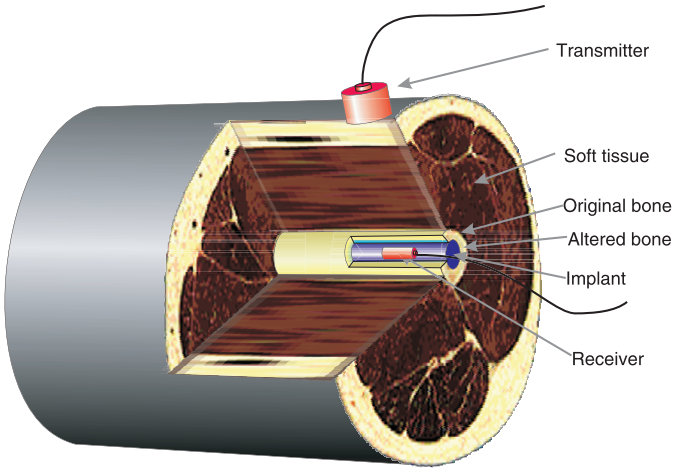


**Figure 1.** Diagram of the experimental setup to be modelled.

These parameters are combined during the different layers and generate a waveform that needs to be processed by a complete inversion scheme. To best measure the velocity and attenuation, we adopt a transmission setup with a low frequency (below the megahertz) ultrasonic pulse containing a wide range of frequencies and a high power of penetration.

Several methods are available to measure bone density, in comparison with which the benefits of ultrasound are that it does not induce ionizing radiation, the technology is inexpensive and more appropriate for continuous and real-time monitoring. It also measures directly elastic constants and density, instead of correlating them to the measured absorption or other indirect physical magnitudes.

We are interested in measuring the elastic properties of the active layer of bone in contact with the implant. The setup herein proposed is depicted in figure 1. In this figure, a section of the leg, crossing the shaft of the hip implant, is presented. An ultrasonic receiver is built in the implant shaft before the surgery. The transmitter is placed on the patient's skin in a similar fashion as with echography.

### *2.2. Forward problem*

A numerical simulation of the experiment is proposed using a finite element (FEM) model of the ultrasonic propagation of the waves through the multilayered solid, which is composed as in the scheme in figure 2. The RF signals compared to the experimental ones during the inverse problem solution are the displacements at the measurement point in the time domain.

A 2D plain strain model is assumed, since the 3D effects are expected to be limited, at least for the purpose of this feasibility study. The boundary conditions are determined by a low frequency ultrasonic beam passing through the layers and measured in a transmission setup by a couple of piezoelectric ultrasonic transducers. The transmitter is modelled by a prescribed traction boundary condition by a normal pressure varying only with time, that is uniform over the transducer contact area. The receiver is modelled by the integral of the normal displacement fields using a constant weighting function over the transducer contact area.

The elastic properties of the layers are taken from figure 3 containing typical values of bulk moduli $K = \frac{E}{3(1-2\nu)} = \rho\left(c_p^2 - \frac{4}{3}c_s^2\right)$. Kallel and Bertrand (1996) use a Poisson ratio

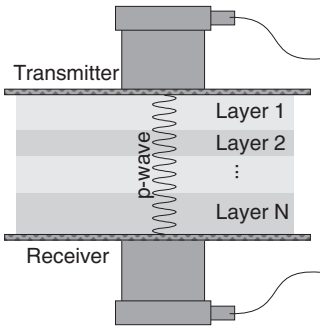


**Figure 2.** Scheme of the setup for the FEM model.

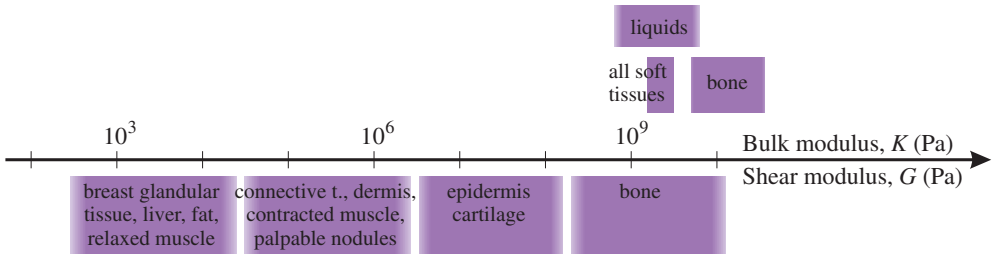


**Figure 3.** Typical range of values of elastic moduli of biological tissues. Adapted from Kallel and Bertrand (1996).

of $\nu = 0.495$, thus relaxing the incompressibility condition ($\nu = 0.5$) and stabilizing the numerical solution. We consider that two constants should be maintained: the bulk wave velocity, which is almost constant through soft tissue and almost equal to the P-wave velocity ($c_p = 1450$ m s$^{-1}$ for fat and $c_p = 1585$ m s$^{-1}$ for muscle, as gathered by Christensen *et al* (1978)), since S-waves are included in the FEM model, and the Young's modulus $E$. The value of the Poisson modulus $\nu$ is uniquely defined as

$$\nu = \frac{\frac{E}{\rho c_p^2} + \sqrt{\left(\frac{E}{\rho c_p^2}\right)^2 - 8\frac{E}{\rho c_p^2}}}{4}. \tag{1}$$

### *2.3. Inverse problem*

The characterization inverse problem or search of the mechanical parameters is carried out with an iterative strategy based on the minimization of some discrepancy of the measured and numerically predicted waveforms $\Phi^x(t)$ and $\Phi(t)$, respectively. The discrepancy is a vector of values or a function that can be discretized (represented by a vector). Since two vectors cannot be compared directly, a scalar number (called cost functional) is derived from them as follows, in order to be able to minimize that discrepancy.

A *residual* $\gamma$ is defined from the misfit or *discrepancy* $\Phi^x - \Phi$ between the measurements:

$$\gamma = (\Phi^x - \Phi). \tag{2}$$

There are many options for designing a cost functional. The necessary conditions are (a) that a full coincidence of prediction and measurement (zero discrepancy) should happen at

the absolute minimum of the cost functional and (b) that the minimum is unique. The L-2 norm, in a standard metric Euclidean space of these residual vectors, is usually a good choice of cost functional, since it naturally fulfils those conditions, and is numerically smooth and well conditioned. This quadratic or least-squares-type definition is also meaningful both in a probabilistic sense and in an algebraic sense, because it is a measure of a distance between bad and good results. The *cost functional* $f$ or fitness function is therefore chosen after a residual vector $\gamma$ as the following integral over the entire recorded time window $T$:

$$f = \frac{1}{2}\int_0^T |\gamma(t)|^2 \, \mathrm{d}t. \tag{3}$$

The parametrization can be defined within the context of inverse problems as a description or characterization of the sought information (i.e. elastic constants characterization) with a reduced set of variables $\mathbf{p} = \{p_i\}$. The issue of parametrization is complex due to the relationship with many considerations of the inverse problem. Many inverse problems are ill-posed: solutions may not exist, they could be unstable and non-converging, or multiple solutions may exist. This is true especially when we are dealing with a large number of parameters. From the conceptual point of view, it can be seen as the most powerful means of inverse problems regularization, since it provides *a priori* information in the form of a strong hypothesis of the possible forms of the sought solutions. The choice of parameters has crucial implications in the convergence, the sensitivity of the result and the decoupling of their dependence to the measurements. In this work, the parameters we adopt are the basic mechanical constants of the set of unknown layers, as well as their number and thickness. This set of variables is normalized to $\hat{p}_i$ by a typical or reference value $p_i^0$, in order to avoid scaling problems,

$$p_i = p_i^0 \, \mathrm{e}^{\hat{p}_i}. \tag{4}$$

At this point, the inverse problem of defect evaluation can be stated as a minimization problem, that can be constrained, as finding $\mathbf{p}$ such that

$$\min f(\mathbf{p}). \tag{5}$$

Figure 4 summarizes the procedure described above, in which the search algorithm is a gradient-based nonlinear optimization algorithm defined as the combination of the Broyden–Fletcher–Goldfarb–Shanno (Dennis and Schnabel 1983, 1996) (BFGS) Hessian update method with a quadratic-cubic line search (LS). Every cost functional evaluation invoked by the optimization algorithm implies the FEM propagation solution of an entire model, with changed parameters. In this scheme we use as parameters the basic elastic constants, Young's modulus and density, of a limited number of bone layers, which produces a reduced set of parameters. These parameters are moreover conditioned by the normalization procedure described above.

## 3. Numerical results

In order to verify the effect of the nanostructured titania coating on the mechanical performance of the new induced bone, some elastic properties have to be quantified at several positions: close to the interface with the coating and far from it.

### *3.1. Methodology*

For determining the feasibility of this technique, we numerically simulate the sensitivity of the visco-elastic and Poisson moduli against noise contents in the waveform and uncertainties with a variety of origins. The linear isotropic mechanical properties are parametrized by a reduced

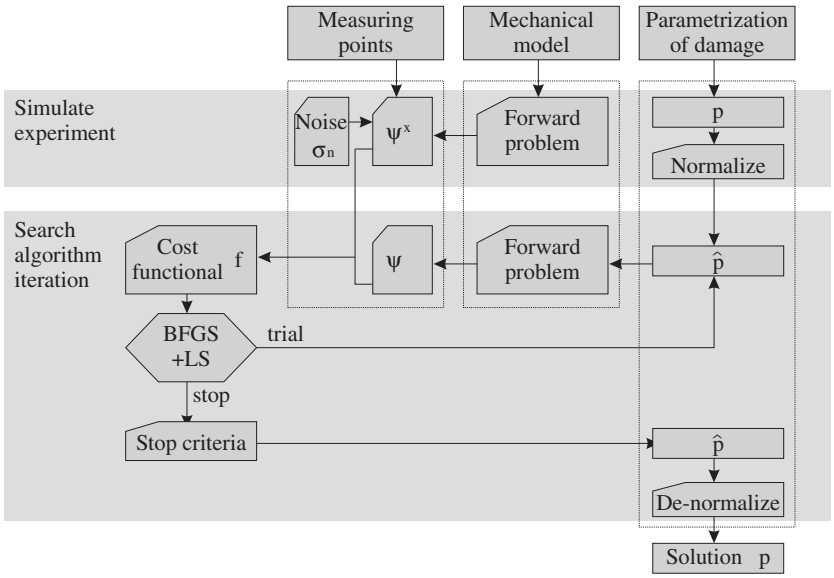


**Figure 4.** Flow chart of the solution of the inverse problem.

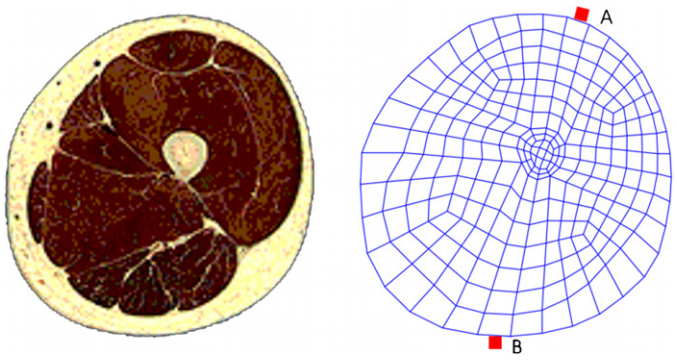


**Figure 5.** Geometry and FEM mesh of the specimen.

set of points of the stress–strain curves. The number of layers and the thickness-to-wavelength ratio are parametrically studied to find the range of maximum sensitivity.

The geometry of the specimen was obtained from high-resolution pictures of a real human body carried out at Washington University in St Louis (Chang 2006). The specimen is taken as a 2D slice of a human leg, crossing the upper part of the femur, and containing the shaft of a hip implant titanium prosthesis. The geometry is shown in figure 5, which is assumed to be divided into four homogeneous and isotropic kinds of materials, whose mechanical properties are assumed to be known as given in table 1. In addition, Rayleigh-type damping is assumed to be $\alpha = 2000f$ (where $f$ is the frequency in kHz) for tissue and $\alpha = 100f$ for the titanium. The excitation central frequency for the tests is 50 kHz and the time window 100 $\mu$s (=5$T$). The FEM mesh is based on the structure depicted in the same figure, which is further refined to adapt to the wavelength of the ultrasonic waves.

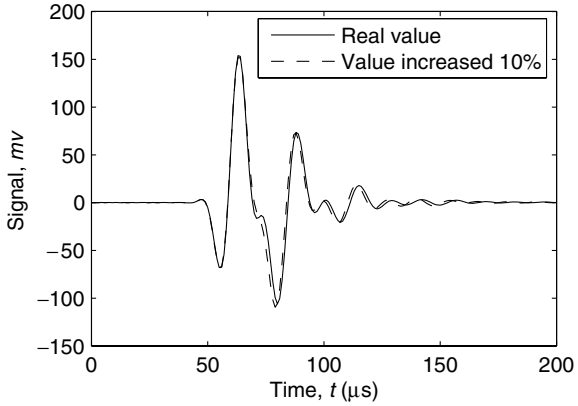


**Figure 6.** Sample of the signal. The sought parameter, which is the elastic modulus of the inner bone layer, is varied by 10%, to verify the magnitude of the variation of the signal.

**Table 1.** Mechanical properties of tissues (from surface and inwards) (Golombeck 2006).

| Material | Graded | Young's modulus $E$ (Pa) | Poisson ratio $\nu$ | Density $\rho$ (kg m$^{-3}$) |
|---|---|---|---|---|
| Fat tissue | Homogeneous | $10 \times 10^6$ | 0.499 14 | 920 |
| Muscle tissue | Homogeneous | $20 \times 10^6$ | 0.498 76 | 1070 |
| Bone tissue | Two-layered | $12 \times 10^9$ | 0.30 | 1260 |
| Titanium | Homogeneous | $114 \times 10^9$ | 0.326 | 4480 |

In the simulations of the experiment, the ultrasonic transmitter is modelled as a point source located at point $A$ in figure 5. The receiver is located opposite to above, at point $B$.

A standard finite element model is constructed using the research academic code FEAP by Taylor (2003). The model is solved by a HHT (Hilbert–Hughes–Taylor) explicit time integration scheme (the conserving alpha method, with parameters $\beta = 0.5, \gamma = 1, \alpha = 0.5$). The time step is related to the central frequency of the input signal $f_c$ by $\Delta t = \frac{0.05}{f_c}$, and the spatial discretization consists of four-noded linear elements of a maximum dimension of around 10% of the smallest wavelength.

A sample of the synthesized signal with two different values (by 10%) of the parameter to be sought shows, in figure 6, that it is clearly sensitive to that change on the bone layer. In order to simulate real measurements, they are synthesized by the same model, but adding a level of noise of 2% of the RMS of the signal. This level of noise is used for the parameter recovery tests.

### *3.2. Sensitivity to noise*

The sensitivity is measured by observing the capacity of the algorithm to show a minimum and verifying its shifting from the true value. For this purpose, the cost functional $f$ is plotted against the values of the input parameter $p$, for an increasing level of noise. The noise is introduced as a signal-to-noise ratio (SNR), by introducing in the recordings a random noise with Gaussian distribution on zero mean and standard deviation defined as a percentage of the RMS of the signal as follows: given an original simulated discrete signal $s(t_i)$, the noisy one $s'(t_i)$ is generated by means of a randomly generated vector $\xi_i$ as

$$s'(t_i) = s(t_i) + \mathrm{SNR} \cdot \xi_i \cdot \mathrm{RMS}(s(t)). \tag{6}$$

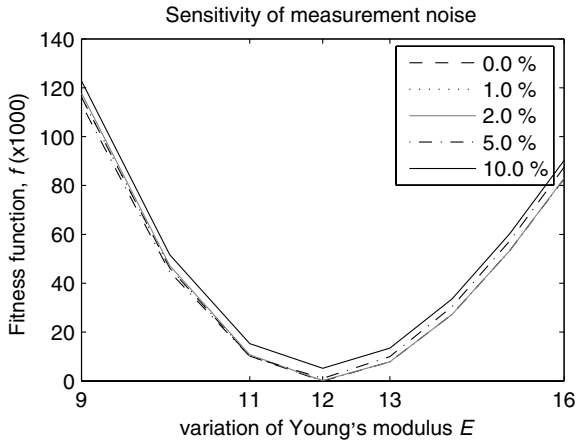


**Figure 7.** Sensitivity to measurement noise. The geometry, mechanical constants and measuring model are defined in section 3.1, table 1 and figure 6.

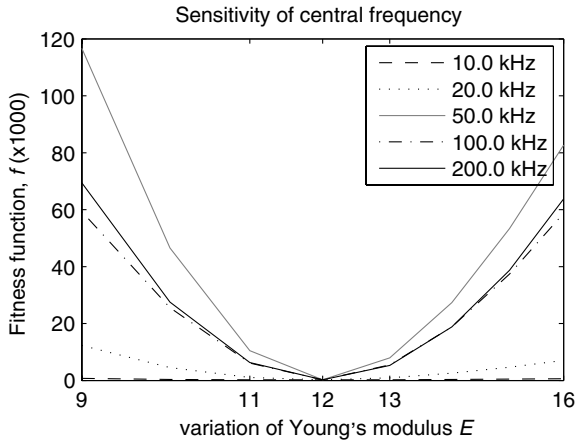


**Figure 8.** Sensitivity to frequency. The geometry, mechanical constants and measuring model are defined in section 3.1, except for the parameter being varied.

The simulated noise is therefore applied directly on the measurements. Figure 7 shows that the technique is highly robust against a high noise level, because the global minimum of the fitness function is not altered after an increase of the noise up to 10%.

### *3.3. Sensitivity to frequency*

The choice of central frequency of the signal should provide a balance between the penetration associated with low frequency and the spatial resolution at high frequency. Since the proposed technique allows us to study at a sub-wavelength resolution, a lower frequency is allowed. Figure 8 shows the sensitivity of the algorithm for a range of frequencies. For this purpose, the cost functional $f$ is plotted against the values of the input parameter $p$, for an increasing frequency. The sensitivity is measured by observing the smoothness of the overall cost

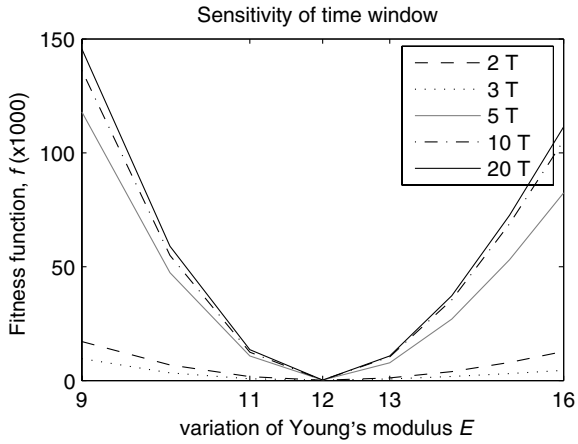


**Figure 9.** Sensitivity to the size of the time window. The geometry, mechanical constants and measuring model are defined in section 3.1.

functional as well as the clarity of the minimum, as it should be found by an optimization algorithm. In the remaining sensitivity tests, no simulated noise is introduced, to better isolate the effect of other parameters. This figure shows that an excitation with a central frequency around 50 kHz provides best contrast. The trend is not monotonic, probably since the attenuation at higher frequencies reduces the amplitude of the signal and hence the signal-to-noise ratio, whereas at lower frequencies the wavelength becomes too large in comparison with the thickness of the investigated bone layer, and therefore little affected by the measured parameter. This reflects the trade-off between penetration and resolution.

### *3.4. Sensitivity to the time window*

The time window chosen for the measurements is chosen as a multiple the period $T$ of the central frequency. The sensitivity to the choice of this value is verified in figure 9. It is shown that the larger the time window the better the sensitivity. This is especially true until $5T$. A reason against using a too long time window is that noise and effects from uncertainties of the model may gain too much magnitude and contaminate the signal after a long time. Hence, a time window of $5T$ is chosen.

### *3.5. Sensitivity to geometry uncertainties*

Figure 10 provides a similar result for errors induced in the geometry of the slice, both for the outer boundary and interfaces between tissues. In particular, the geometry error is defined by moving the master nodes that define the geometry (a total of 78) in a random direction and to a random distance with a normal distribution of zero mean and standard deviation equal to the indicated percentage of a standard length. The method is extremely sensitive to uncertainties in the geometry, which is a major limitation. This suggests the need to immobilize the specimen while measuring, or alternatively, to combine this measurement with a real-time echographic imaging of the specimen. The spatial resolution required for the imaging system is readily given by the percentage of error in geometry that corresponds to a desired level of error in the output parameters. For instance, if the admissible deviation in the output elastic parameter

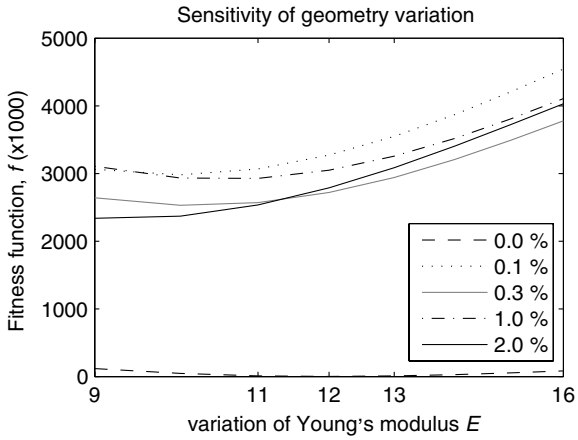


**Figure 10.** Sensitivity to geometry errors. The geometry, mechanical constants and measuring model are defined in section 3.1.

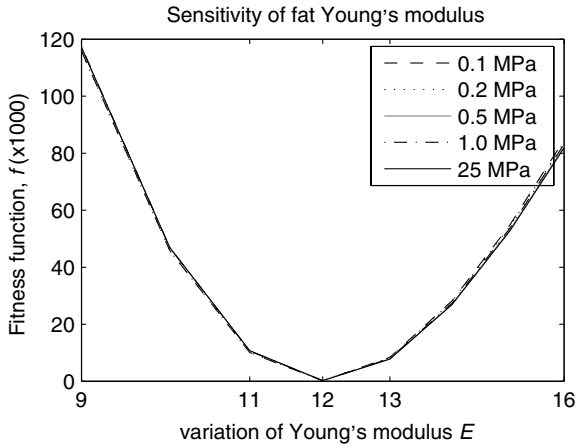


**Figure 11.** Sensitivity to uncertainty in the fat Young's modulus. The geometry, mechanical constants and measuring model are defined in section 3.1.

is 5%, which corresponds to the 0.1% geometry error curve in figure 10, an image with geometrical resolution of the order of 0.1% $\times 100$ mm $\simeq$ 0.1 mm should be used.

### *3.6. Sensitivity to model uncertainties*

Figure 11 analyses the variation of the bone stiffness when the original mechanical parameters of the fat tissue are varied. The recovered parameters appear to be little sensitive to a wide range of uncertainties. Figure 12 shows an equivalent result for the muscle Young's modulus, and a similar conclusion can be drawn.

The present technique succeeds in becoming sufficiently independent of uncertainties in the soft tissue mechanical properties (which may vary by a factor of 10 without significantly

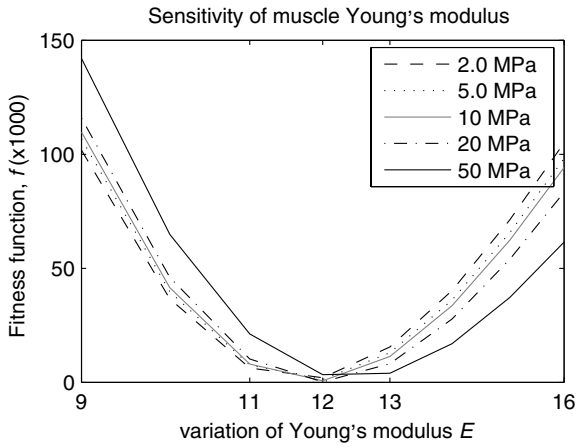


**Figure 12.** Sensitivity to uncertainty in the muscle Young's modulus. The geometry, mechanical constants and measuring model are defined in section 3.1.

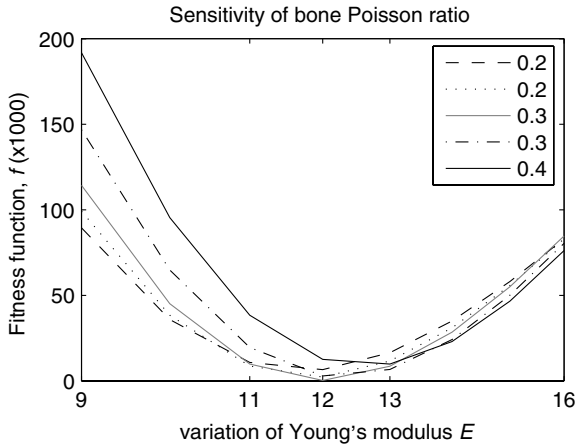


**Figure 13.** Sensitivity to uncertainty in the bone Poisson ratio. The geometry, mechanical constants and measuring model are defined in section 3.1.

varying the prediction in bone elastic modulus). These tissue properties may vary rapidly due to movements and exchange of fluids.

The three remaining linear elastic constants, the Poisson ratio and the density of the bone and the Rayleigh damping, are studied similarly in figures 13–15.

This approach remains sufficiently insensitive to bone Poisson modulus, but not to bone density. This indicates that its density is a variable that should also be predicted in coupling with the Young's modulus, both of which indicate the quality of the bone. The method is also highly sensitive to uncertainties in the Rayleigh damping ratio, which is a second limitation of the technique. To overcome this, some procedure should be used to determine this value and calibrate the measurements in advance, by recovering these unknown parameters at the calibration stage.

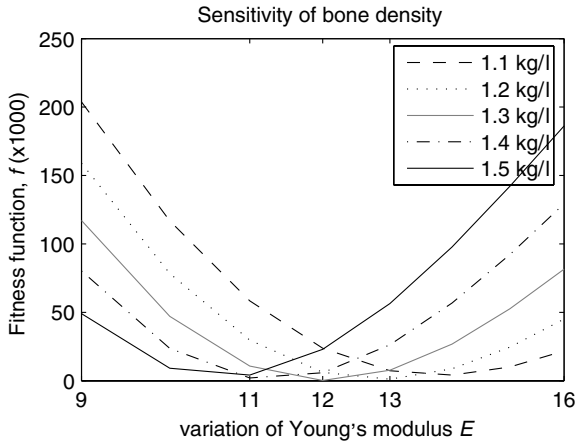


**Figure 14.** Sensitivity to uncertainty in the bone density. The geometry, mechanical constants and measuring model are defined in section 3.1.

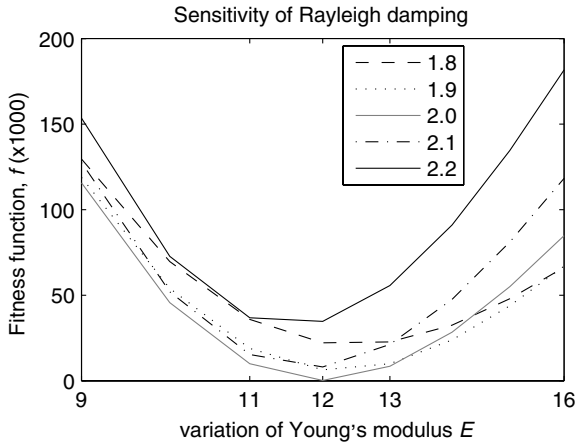


**Figure 15.** Sensitivity to uncertainty in the Rayleigh damping. The geometry, mechanical constants and measuring model are defined in section 3.1.

### *3.7. Inverse problem results*

In order to finally recover the mechanical performance of the new bone layer induced on the nanostructured titania coating, three inverse problems are solved, in which the Elastic modulus and density distribution of the inner bone layer are identified. This distribution is discretized into concentrical layers at uniform spacing, interpolated from the real geometry. The inner layer (i.e. the one in contact with the implant) is therefore assumed to be first to change its properties due to the nanostructured $TiO_2$ coating.

The first inverse problem identifies only the elastic modulus in two layers (inner and outer, identifying a total of two parameters) in figure 16. On the right-hand side of the figure, the normalized values of the parameters are represented as the iterative minimization algorithm progresses, until its convergence. The right-hand side of the figure presents a greyscale map

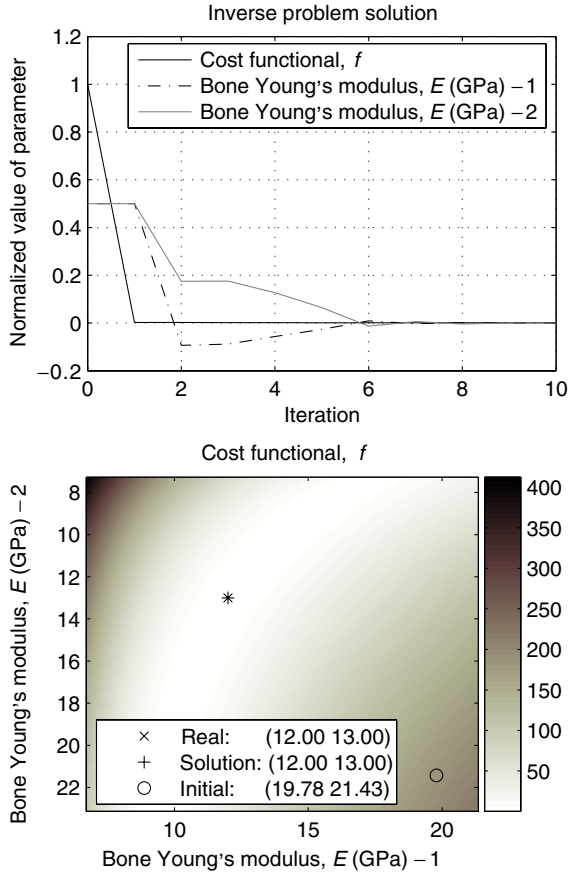


**Figure 16.** Inverse problem of two parameters: Young's modulus for two internal layers of bone. Top: evolution of the search algorithm. Bottom: map of values of cost functional $f$ for every combination of trial parameters.

of the value of the cost functional $f$ for each combination of parameters. Figure 17 also presents the solution of an inverse problem of identifying two parameters: Young's modulus and density for just one internal layer of bone, assuming the outer layer remains unchanged.

Finally, figure 18 presents the solution of an inverse problem of identifying six parameters: Young's modulus and density for three internal layers of bone. The first one is in contact with the nanostructured titania coating and the third is away from it. This distribution would allow us to monitor the relative variations and correlate them with the efficiency of titania.

The stability of the inverse problem solution can be evaluated from the uniformity and lack of local minima in the cost functional (greyscale images in figures 16 and 17) and also from the successful parameter estimation from far initial guesses (50% away from the real values). In the case of a large number of parameters, that typically unstabilize the inverse problem solutions, a three-layer and six-parameter solution is obtained with errors around 5%. In all cases, a good convergence is observed in spite of the simulated level of 2% SNR on measurements, which proves the theoretical feasibility of this technique to monitor elastic properties inside bone.

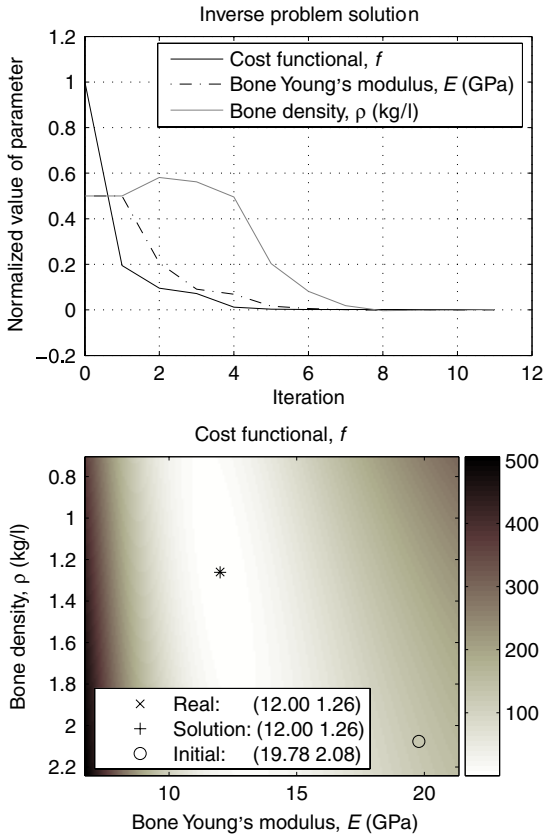


**Figure 17.** Inverse problem of two parameters: Young's modulus and density for one internal layer of bone. Left: evolution of the search algorithm. Right: map of values of cost functional $f$ for every combination of trial parameters.

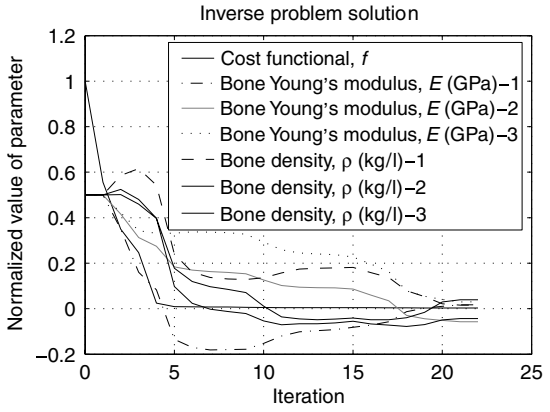


**Figure 18.** Inverse problem of six parameters: Young's modulus and density for three internal layers of bone. Evolution of the search algorithm.

## 4. Conclusions

The induced growth of bone by nanostructured implant coatings is a promising application of nanomaterials. This growth is currently studied by material science techniques, but a measurement of the bone growth in a real *in vivo* body and in real time is ultimately required to assess the mechanical strength of the resulting skeletal structure.

A technique to monitor the bone distribution of mechanical properties by ultrasonic transmission and solution of the inverse problem is proposed. The ultrasonic transmitter is placed outside the body, and the receiver is embedded in the implant. A feasibility study by numerical simulations is done to identify the constraints and applicability of the technique. The benefits of ultrasound are (i) it does not produce ionizing radiation, (ii) the technology is inexpensive, (iii) it is therefore more appropriate for real-time monitoring and (iv) it also measures directly elastic constants and density, instead of correlating them to the measured absorption.

It is found that a sufficient precision on the value of the Young's modulus of a bone layer around the implant is obtained. This value is sufficiently independent of the uncertainties in the soft tissue mechanical properties. On the other hand, the technique is limited in that a high precision knowledge is required of the geometry of the model as well as the damping parameters and Poisson ratio of the bone. The extent of this limitation is quantified and is affordable by considering a proper calibration of those parameters in the experimental design.

The presented approach for elastic tissue characterization can be extended to a great variety of applications in medical diagnosis related to elastography, where quantified elastic constants can be correlated with pathology conditions. This extension may be limited by the requirements in the *a priori* knowledge of geometrical and mechanical parameters, as commented above, but may provide new and useful information for clinical applications.

## Acknowledgments

Javier García-Martínez wishes to thank the Ministerio de Educación y Ciencia (Spain) for a Ramón y Cajal contract, and the authors are grateful to Generalitat Valenciana for grant INV05-10. The authors are grateful to the Washington University in St Louis for the high-resolution images from the Visible Human Project.

## References

Bayoumi F M and Ateya B G 2006 Formation of self-organized titania nano-tubes by dealloying and anodic oxidation *Electrochem. Commun.* **8** 38–44

Branemark P I, Hansson H A, Adell R, Breine U, Lindstrom J, Hallen O and Ohman A 1977 Osseointegrated implants in the treatment of the edentulous jaw. Experience from a 10-year period *J. Plast. Reconstr. Surg.* **11** 39

Chang M 2006 *A Guided Tour of the Visible Human* (St Louis, MO: Washington University in St Louis) (http://medicine.wustl.edu, http://www.madsci.org/∼lynn/VH/)

Christensen E E, Curry T S and Dowdey J E 1978 *Introduction to the Physics of Diagnostic Radiology* (Philadelphia, PA: Lea & Febeger)

Dennis J E Jr and Schnabel R B 1983, 1996 *Numerical Methods for Unconstrained Optimization and Nonlinear Equations* (Philadelphia, PA: SIAM)

de Oliveira P T and Nancy A 2004 Nanotexturing of titanium-based surfaces upregulates expression of bone sialoprotein and osteopontin by cultured osteogenic cells *Biomaterials* **25** 403–13

Dieudonné S C, van den Dolder J, de Ruijter J E, Paldan H, Peltola T, van't Hof M A, Happonen R P and Cansen J A 2002 Osteoblast differentiation of bone marrow stromal cells cultured on silica gel and sol–gel-derived titania *Biomaterials* **23** 3041–51

Doyley M M, Srinivasan S, Pendergrass S A, Wu Z and Ophir J 2005 Comparative evaluation of strain-based and model-based modulus elastography *Ultrasound Med. Biol.* **31** 787–802

Golombeck M A 2006 Institut für Biomedizinische Technik http://www-ibt.etec.uni-karlsruhe.de/people/mag

Gonzalez M H and Mekhail A O 2004 The failed total knee arthroplasty: evaluation and etiology *J. Am. Acad. Orthop. Surg.* **12** 434–46

Gutwein L G and Webster T J 2003 Increased viable osteoblast density in the presence of nanophase compared to conventional alumina and titania particles *Biomaterials* **25** 4175–83

Hall T J 2003 Aapm/rsna physics tutorial for residents: topics in us: beyond the basics: elasticity imaging with us *Radiographics* **23** 1657–71

Haydon C M, Mehin R, Burnett S, Rorabeck C H, Bourne R B, McCalden R W and MacDonald S J 2004 Revision: total hip arthroplasty with use of a cemented femoral component. Results at a mean of ten years *J. Bone Joint Surg. Am.* **86A** 1179–85

Hazan R, Brener R and Oron U 1993 Bone growth to metal implants is regulated by their surface chemical properties *Biomaterials* **18** 570–4

Hill C R, Bamber J C and Haar G R (ed) 2004 *Physical Principles of Medical Ultrasonics* 2nd edn (New York: Wiley)

Kallel F and Bertrand M 1996 Tissue elasticity reconstruction using linear perturbation method *IEEE Trans. Med. Imaging* **15** 299–313

Keshmiri M and Troczynski R 2003 Apatite formation on $TiO_2$ anatase microspheres *Non-Cryst. Solids* **324** 289–94

Konofagou E E 2004 Quo vadis elastography? *Ultrasonics* **42** 331–6

Lear Swan E E, Popat K C, Grimes C A and Desai T A 2005 Fabrication and evaluation of nanoporous alumina membranes for osteoblast culture *J. Biomed. Mater. Res.* **72A** 288

Lee J-H, Kim S-E, Kim Y-J, Chi C-S and Oh H-J 2006 Effects of microstructure of anodic titania on the formation of bioactive compounds *Mater. Chem. Phys.* **98** 39–43

Miga M I 2003 A new approach to elastography using mutual information and finite elements *Phys. Med. Biol.* **48** 467–80

National Osteoporosis Foundation 2003 http://www.nof.org

Ophir J, Kallel F, Varghese T, Konofagou E E, Alam S K, Krouskop T, Garra B and Righetti R 2002b Elastography *C. R. Acad. Sci. Paris: Appl. Phys.* **2** 1193–11

Ophir J *et al* 2002a Elastography: imaging the elastic properties of soft tissues with ultrasound *J. Med. Ultrason.* **29** 155–71

Palin E, Liu H and Webster T J 2005 Mimicking the nanofeatures of bone increases bone-forming cell adhesion and proliferation *Nanotechnology* **16** 1828–35

Righetti R, Ophir J, Srinivasan S and Krouskop T A 2004 The feasibility of using elastography for imaging the Poisson's ratio in porous media *Ultrasound Med. Biol.* **30** 215–28

Taylor R L 2003 *Feap—A Finite Element Analysis Program* version 7.5 (rlt@cs.berkeley.edu)

US Census Bureau 2003 http://www.census.gov

Webster T J, Schadler L S, Siegel R W and Bizios R 2001a Mechanisms of enhanced osteoblast adhesion on nanophase alumina involve vitronectin *Tissue Eng.* **7** 291–301

Webster T J, Siegel R W and Bizios R 1999 Osteoblast adhesion on nanophase ceramics *Biomaterials* **20** 1221–7

Webster T J, Siegel R W and Bizios R 2000 Enhanced functions of osteoblasts on nanophase ceramics *Biomaterials* **21** 1803–10

Webster T J, Siegel R W and Bizios R 2001b Nanoceramic surface roughness enhances osteoblast and osteoclast functions for improved orthopaedic/dental implant efficacy *Scr. Mater.* **44** 1639–42

Wells P N T 2006 Ultrasound imaging *Phys. Med. Biol.* **51** R83–98

Zhu S, Dreyer T, Liebler M, Riedlinger R, Preminger G M and Zhong P 2004 Reduction of tissue injury in shock-wave lithotripsy by using an acoustic diode *Ultrasound Med. Biol.* **30** 675–82